

Strain rate-dependent tensile response of glassy silicon nanowires studied by accelerated atomistic simulations

Cite as: *J. Appl. Phys.* **130**, 085105 (2021); <https://doi.org/10.1063/5.0060136>

Submitted: 15 June 2021 . Accepted: 02 August 2021 . Published Online: 27 August 2021

 Yanming Zhang,  Penghui Cao,  Binghui Deng, et al.

COLLECTIONS

 This paper was selected as Featured



[View Online](#)



[Export Citation](#)



[CrossMark](#)

ARTICLES YOU MAY BE INTERESTED IN

Machine learning-based data processing technique for time-domain thermoreflectance (TDTR) measurements

Journal of Applied Physics **130**, 084901 (2021); <https://doi.org/10.1063/5.0057796>

Plasma processing for advanced microelectronics beyond CMOS

Journal of Applied Physics **130**, 080901 (2021); <https://doi.org/10.1063/5.0053666>

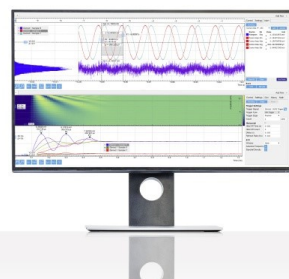
Defects in multilayer MoS₂ grown by pulsed laser deposition and their impact on electronic structure

Journal of Applied Physics **130**, 084303 (2021); <https://doi.org/10.1063/5.0057165>

Challenge us.

What are your needs for
periodic signal detection?

 Watch



Zurich
Instruments

Strain rate-dependent tensile response of glassy silicon nanowires studied by accelerated atomistic simulations



Cite as: J. Appl. Phys. 130, 085105 (2021); doi: 10.1063/5.0060136

Submitted: 15 June 2021 · Accepted: 2 August 2021 ·

Published Online: 27 August 2021



View Online



Export Citation



CrossMark

Yanming Zhang,¹ Penghui Cao,² Binhui Deng,³ Liping Huang,¹ and Yunfeng Shi^{1,a)}

AFFILIATIONS

¹Department of Materials Science and Engineering, Rensselaer Polytechnic Institute, Troy, New York 12180, USA

²Department of Mechanical and Aerospace Engineering, University of California, Irvine, California 92697, USA

³Manufacturing Technology and Engineering, Corning Incorporated, Corning, New York 14830, USA

^{a)}Author to whom correspondence should be addressed: shiy2@rpi.edu

ABSTRACT

Mechanical properties of glassy nanowires have been intensively investigated recently by both nanomechanical experiments and atomic-level simulations. Unfortunately, there exists a huge gap in the strain rate of the nanomechanical tests between experiments and simulations, which makes it difficult to compare results even for the same material system. Using accelerated atomistic simulations based on a self-learning metabasin escape algorithm, here, we report the tensile mechanical properties of amorphous Stillinger–Weber silicon nanowires with different intrinsic ductility under strain rates ranging from 10^{10} to 10^{-1} s $^{-1}$. It is found that both brittle and ductile glassy silicon nanowires display weakened strength with a decreasing strain rate, in agreement with the cooperative shear model. Moreover, as the strain rate decreases, the amount of plasticity remains unchanged for the brittle nanowires, yet it decreases for the ductile ones. Such deteriorated plasticity in ductile glassy nanowires is caused by enhanced strain localization at low strain rates. Lastly, we show that via the distance matrix of nonaffine displacement, a more hierarchical potential energy landscape is responsible for the higher strain localization propensity in ductile silicon glassy nanowires.

Published under an exclusive license by AIP Publishing. <https://doi.org/10.1063/5.0060136>

INTRODUCTION

Amorphous nanowires have drawn great attention in past decades due to their promising applications in the fields of energy, optics, nanoelectronics, and engineering.^{1–5} Among the various attractive material properties of glassy nanowires, their mechanical properties are under intensive investigations as mechanical integrity is a prerequisite to fulfill other functionalities.^{6–10} Although generally exhibiting zero ductility under unconstrained loading conditions in the bulk form, both metallic and oxide glasses were recently reported to display substantial tensile ductility at the nanoscale,^{11,12} depending on the intrinsic ductility,^{13,14} sample size,^{15–17} or surface conditions.^{11,18}

One particularly intriguing puzzle is how the applied strain rate affects deformation mechanisms and, thus, the mechanical properties of glassy nanowires.^{19,20} Solutions to this puzzle will not only deepen our understanding of dynamics of local plastic

events^{21–24} but may also open new windows for glasses in emerging devices such as nanoresonators and nanoswitches.^{25–27} Traditionally, to explore the rate-dependent mechanical response of glass nanowires, both high-strain-rate molecular dynamics simulations^{28–32} (mostly $>10^8$ s $^{-1}$) and low strain-rate experimental nanomechanical tests^{7,12,33,34} (mostly $<10^0$ s $^{-1}$) were used. However, a huge gap in the timescale between simulations and experiments often leads to discrepancies in understanding the plasticity of glass nanowires, especially when the deformation mechanism is largely strain rate dependent.^{35,36} Particularly, recent simulations^{28,30} and theories³⁷ show that a higher strain rate promotes plastic deformation, while experiments^{12,33} reveal that a higher strain rate hinders plastic events in glassy nanowires. In addition, the differences in both the sample size and the intrinsic ductility of glasses may also contribute to the inconsistency. Therefore, a complete understanding requires conducting mechanical tests covering timescales over ten orders of magnitude for glassy nanowires with controllable intrinsic ductility and sample size.

Recently, substantial progress toward experimental timescales has been made via conducting accelerated atomistic simulations including the activation-relaxation technique,³⁸ the dimer method,³⁹ hyperdynamics,⁴⁰ temperature accelerated dynamics,⁴¹ and the autonomous basin climbing (ABC) method.^{42,43} Particularly, a novel atomic simulation technique, called the self-learning metabasin escape (SLME) algorithm, has demonstrated its capability in conducting mechanical tests at experimental timescales.^{44–46} Encouragingly, this technique has been successfully applied to reveal the strain-rate-dependent ductile to brittle transition in bicrystalline nanowires,⁴⁷ to understand the mechanisms of creep in glasses at experimental timescales,⁴⁸ and to uncover the interplay of stress-activation and thermal-driven local rearrangements inside glasses under shear strain rates spanning ten orders of magnitude.⁴⁹

Using the SLME technique, we conducted accelerated atomistic simulations under a tensile strain rate from 10^{11} to 10^{-1} s $^{-1}$ for two model amorphous silicon nanowires (one nanowire is intrinsically ductile, while the other is intrinsically brittle). We analyzed the strain-rate-dependent strength, yield strain, and plasticity for brittle and ductile glasses, as well as the underlying atomic-level deformations mechanisms. Particularly, we observed an intrinsic difference in the strain-rate dependence of plasticity between brittle and ductile nanowires, which is owing to their difference in hierarchies of their potential energy landscape (PEL).

SIMULATION METHODOLOGIES

Classical molecular dynamics simulations

We carried out classical molecular dynamics (CMD) simulations in LAMMPS package⁵⁰ using the Velocity-Verlet algorithm integrated with a time step of 1 fs. To control the pressure and temperature of the glassy systems, both Nose-Hoover barostat and thermostat^{51,52} were used.

Model amorphous silicon systems were studied here, in which the particle interactions are defined by the Stillinger-Webber (SW) potential.⁵³ To investigate the strain-rate effect on the mechanical response of both ductile and brittle glassy nanowires, we tuned the prefactor λ of the angular interaction following the previous strategy.^{14,54,55} Notably, the higher the λ value is, the stronger the bond angle constraint is, and the more brittle the model amorphous silicon behaves. Here, we used $\lambda = 25$ and $\lambda = 33$ to mimic the mechanical behavior of ductile and brittle glasses, respectively. To prepare the glass nanowires, we first quenched bulk glass samples from high temperature melt (5000 K) to room temperature (300 K) at a cooling rate of 5 K/ps under zero pressure. Nanowires were then directly cut from the bulk samples and relaxed at room temperature for ~ 0.5 ns. The final sample size of the nanowires is ~ 4 nm in diameter and 13 nm in length (consisting of ~ 8000 Si atoms). To investigate the mechanical properties of the nanowires, uniaxial tension tests with strain rates ranging from 10^{10} to 10^6 s $^{-1}$ were applied along the axial direction using classical MD simulation methods. Periodic boundary conditions were applied along the axial direction during uniaxial tension tests, while 1 nm vacuum was added in the lateral dimensions to avoid the interactions between a nanowire and its periodic images. The visualization software OVITO⁵⁶ was used to generate simulation snapshots and

animations and calculate the local atomic strain based on the method proposed by Falk and Langer.⁵⁷

Accelerated atomistic simulations

We carried out accelerated atomistic modeling using the recently developed SLME algorithm by Cao *et al.*,⁴⁴ which is a modified and more computationally efficient version of the ABC method originally proposed by Yip and co-workers.^{42,58} Specifically, the SLME algorithm employs a self-generated and self-reconstructed penalty function to assist the system escaping from a given local energy basin on the PEL; hence, the transition pathways with high activation energy barriers (Q_0) can be explored. Therefore, the mechanical properties under strain rates in the range of conventional mechanical testing experiments can be reached, which is not accessible in CMD simulations.^{59,60}

Following the previous publications,^{44,47} the procedure of accelerated atomistic simulation is briefly described below. We first applied a small tensile strain increment of 0.0001 to the sample and then conducted the steepest descent energy minimization⁶¹ to bring the system to the nearest local minimum. Next, the activation trajectories starting from this local minimum were sampled by the SLME algorithm.⁴⁴ Once an activation barrier is greater than a prescribed barrier Q_0 , the sampling along this candidate trajectory finishes. Thus, we can identify a series of local energy minima and saddle points where the transition-state trajectories are generated. Finally, the activation pathway and the corresponding local minimum of choice under the strain increment are determined based on the Metropolis algorithm.⁶² We repeated the above procedure using a constant barrier Q_0 until the final fracture occurred such that the imposed strain rate can be kept constant. Note that to conduct a lower strain-rate test, a higher Q_0 is required, given that the direct connection between activation potential energy barriers (Q_0) and strain rates is made using the transition-state theory^{47,49,63,64} as shown below:

$$\dot{\varepsilon} = \dot{\varepsilon}_0 \exp\left(-\frac{(1 - a(T))^* Q_0}{k_B T}\right), \quad (1)$$

where k_B and T are the Boltzmann constant and temperature, respectively, while $\dot{\varepsilon}_0$ and $a(T)$ are the characteristic strain rate and fitting constant between activation potential energy and activation free energy, respectively.

Figure 1 shows that the mechanical properties of brittle and ductile glassy nanowires from SLME and CMD simulations are generally consistent within the strain rates accessible by the CMD. By comparing the ultimate tensile strength from CMD and SLME simulations, $\dot{\varepsilon}_0$ and $a(T)$ of the brittle and ductile glasses were calculated to be 2.5×10^{10} s $^{-1}$, 0.990 and 1.28×10^{11} s $^{-1}$, 0.993, respectively.

RESULTS

By conducting accelerated atomistic simulations based on the SLME algorithm, we first systematically investigated the tensile response of the brittle and ductile glassy nanowires under strain rates spanning over ten orders of magnitude. For the brittle nanowire ($\lambda = 33$) shown in Fig. 2(a), both the ultimate tensile strength

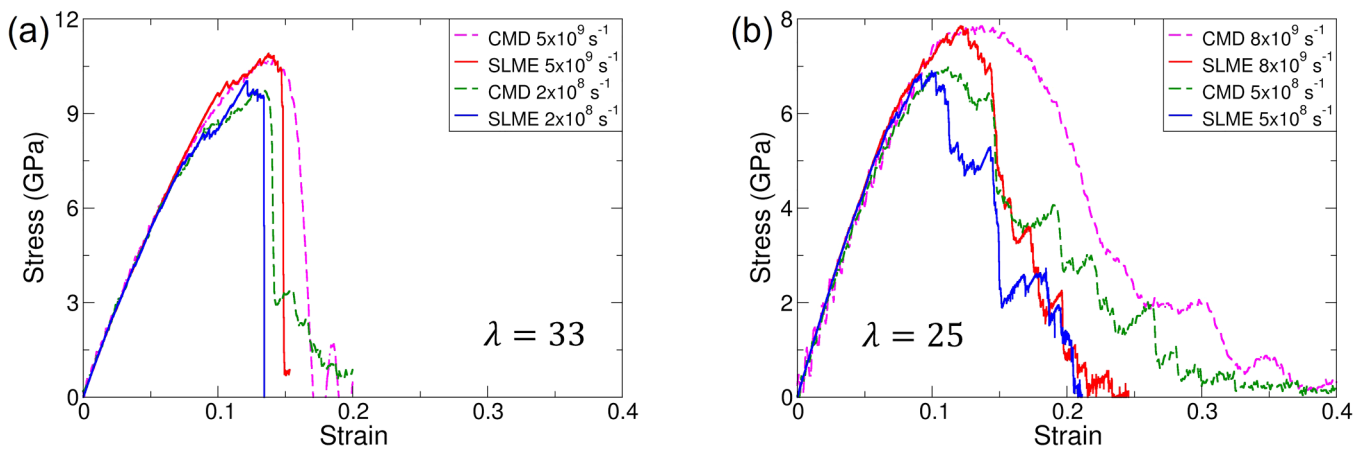


FIG. 1. Stress-strain curves from accelerated atomistic simulations (SLME) and classical molecular dynamics (CMD) for (a) brittle ($\lambda = 33$) and (b) ductile ($\lambda = 25$) glassy nanowires.

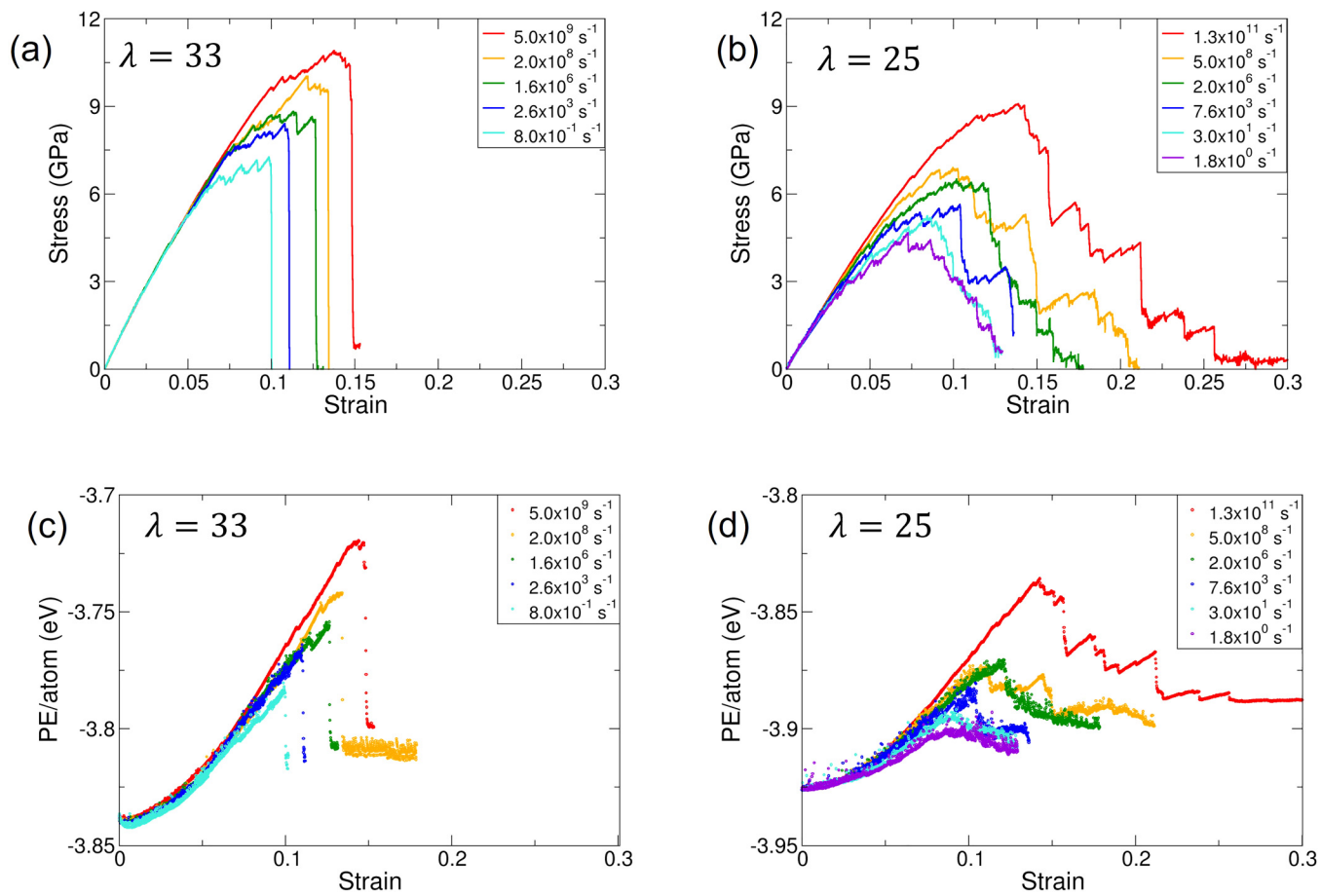


FIG. 2. Tensile stress-strain curves of (a) brittle ($\lambda = 33$) and (b) ductile ($\lambda = 25$) glassy nanowires under different loading rates from accelerated atomistic simulations based on the SLME algorithm. Potential energy (PE) as a function of strain for (c) brittle and (d) ductile glassy nanowires under different loading rates.

(UTS) and the failure strain reduce, while Young's modulus stays roughly the same as the applied strain rate decreases from 5×10^9 to $8 \times 10^{-1} \text{ s}^{-1}$. The strain rate dependency of various mechanical properties will be shown and discussed later in this section. In addition, serrations in the stress-strain curves become more visible as the strain rate reduces, which indicates an increase in the degree of strain localization.^{65,66} Under the same amount of strain, the potential energy (PE) in Fig. 2(c) decreases slightly as the strain rate reduces, suggesting that a lower energy part of the PEL is sampled.

As for the ductile glass ($\lambda = 25$), both the UTS and the failure strain also decrease when the applied strain rate reduces from 1.3×10^{11} to $1.8 \times 10^0 \text{ s}^{-1}$, as shown in Fig. 2(b). Before the UTS is

reached, the ductile nanowires exhibit more obvious serrations with a reducing strain rate as compared with their brittle counterparts. Similar to the brittle glass, more stable inherent structures in the PEL are sampled at lower loading rates, indicated by the lower PE values shown in Fig. 2(d).

To further understand the deformation behavior of the brittle and ductile nanowires over such a broad strain rate range, we calculated the atomic shear deformation of samples under representative strain rates, as shown in Fig. 3. In terms of plastic behavior, the local shear deformation inside the brittle nanowires becomes more heterogeneously distributed as the strain rate decreases, as in Fig. 3(a). Likewise, a noticeable strain localization behavior is also observed in the ductile samples, as shown in Fig. 3(b).

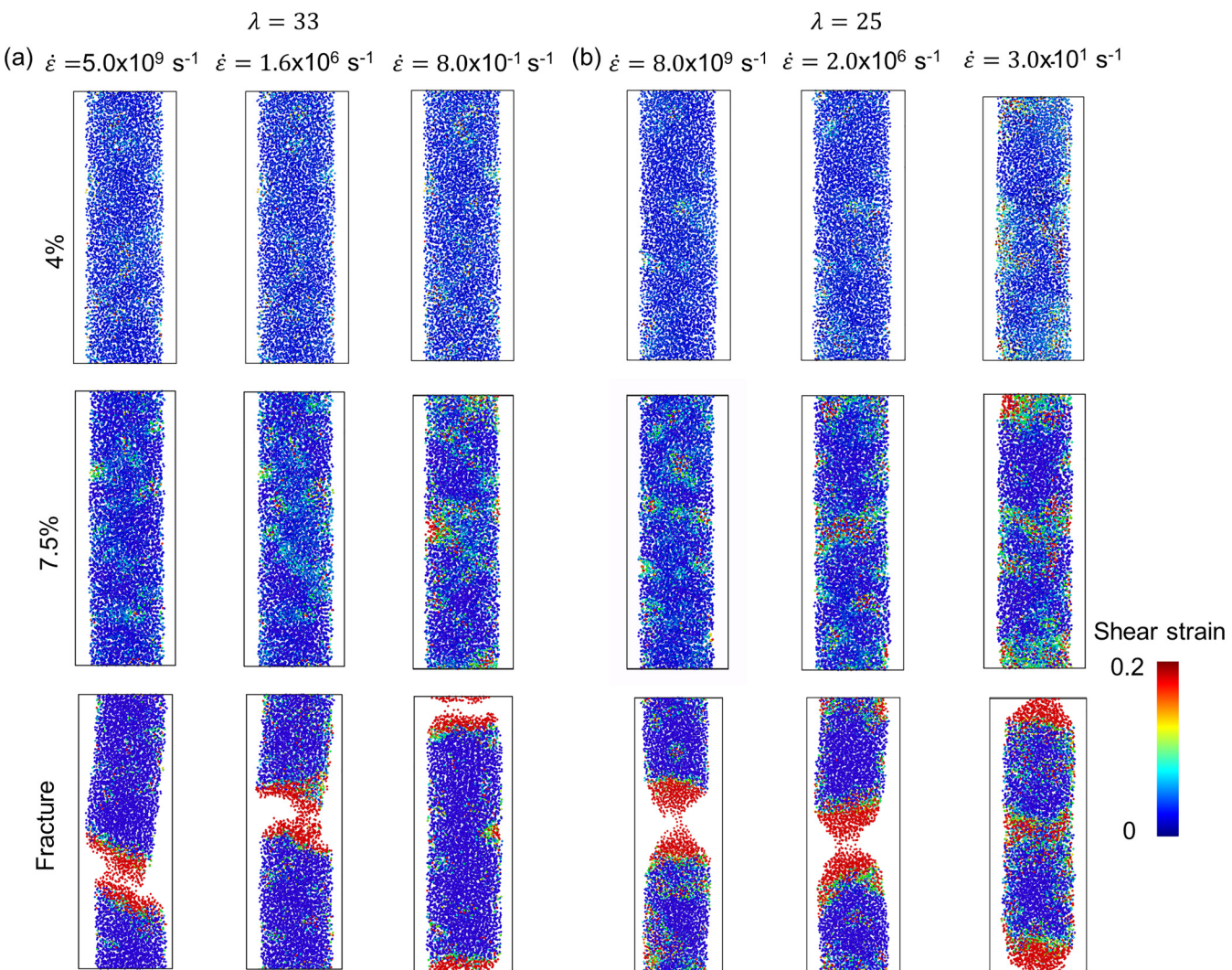


FIG. 3. Deformation snapshots and failure morphologies at selective strain rates for (a) brittle ($\lambda = 33$) and (b) ductile ($\lambda = 25$) glassy nanowires. Atoms are color coded based on their local shear strain.

This pronounced strain localization behavior seems to be the origin of deteriorated mechanical properties, which will be discussed in detail later. In terms of the final failure modes of the glassy nanowires, the brittle nanowires change from shear fracture to cleavage as the strain rate decreases. The shear fracture creates more surface, hence requiring high enough stored elastic energy, which is possible at the highest loading rate. In contrast, fracture is preceded by necking instead of shear banding in the ductile nanowires regardless of the loading rate. The necking behavior in the ductile nanowires is due to the small sample size, which has been revealed in both simulations and experiments.^{16,18}

Next, we systematically calculated the various mechanical properties of the brittle and ductile nanowires under different strain rates. As shown in Fig. 4(a), Young's modulus of both brittle and ductile glassy nanowires calculated from accelerated atomistic simulations (SLME) decreases very slightly with a decreasing strain rate. Within the strain rates accessible to CMD simulations, the computed Young's modulus is well comparable with the SLME results. Poisson's ratio of the brittle glass is lower than that of the ductile nanowires, as seen in Fig. 4(b). This is reasonable, as Poisson's ratio was found to be a good indicator of the intrinsic ductility of glassy materials.^{13,67} As an elastic property, Poisson's ratio of both brittle and ductile nanowires is not sensitive to the strain rate. Figures 4(c)–4(d) show that the yield strength and the UTS both decrease as the strain rate decreases. The strain-rate sensitivity (m) can be computed with the following equation:^{7,68}

$$m = \frac{\partial \ln \sigma}{\partial \ln \dot{\epsilon}}. \quad (2)$$

In terms of the yield strength, m for brittle ($\lambda = 33$) and ductile ($\lambda = 25$) nanowires equal to 0.0085 and 0.0267, respectively. Meanwhile, the m of the UTS for the brittle and ductile samples are 0.0168 and 0.0235, respectively. Therefore, the ductile nanowire displays a much higher sensitivity with respect to the strain rate. The apparent activation volume (V^*) at the point of yielding can also be computed:^{7,69}

$$V^* = k_B T \frac{\partial \ln \dot{\epsilon}}{\partial \sigma}, \quad (3)$$

where k_B and T are the Boltzmann constant and temperature, respectively. The V^* at the yield point of the brittle nanowire is calculated to be 66.17 \AA^3 , which is almost twice that of the ductile nanowire ($V^* = 36.96 \text{ \AA}^3$). The higher activation volume requires a larger population of cooperatively rearranged atoms for plastic deformation, which inhibits shear flow in the brittle glass, resulting in its intrinsic brittleness. At the UTS, the V^* of the brittle and ductile nanowires is reduced to 27.53 and 26.99 \AA^3 , respectively, presumably due to the loss of structural stability caused by stress-induced softening. In addition, the yield strength is fitted with the cooperative shear model^{29,70,71} below, and the fitting constants can be found in Table I,

$$\sigma = \sigma_0 \left(1 - \left(\frac{k_B T}{W_{T_g} G_{T_g}} \ln \left(\frac{w'_0}{\dot{\epsilon}} \right) \right)^{\frac{2}{3}} \right), \quad (4)$$

where σ_0 is the yield strength without thermal activation, W_{T_g} is the activation energy barrier at glass transition temperature (T_g) and depends weakly on temperature below T_g , $\frac{G_T}{G_{T_g}}$ is the ratio of shear modulus at room temperature and T_g , hence close to be unit when omitting thermal expansion, and w'_0 is a fitting constant related to the critical frequency of shear phonons.

It is shown that the activation energy barrier for yielding (W_{T_g}) in the ductile nanowire is less than one third of that of the brittle one; thus, the former can be more easily deformed under loading conditions. Meanwhile, the activation energy barrier for yielding in the model brittle and ductile nanowires investigated here generally agrees with previous estimations for silica glass ($W_{T_g} \sim 12 \times 10^{-19} \text{ J}$)⁷² and metallic glasses ($W_{T_g} \sim 12 \times 10^{-19} \text{ J}$),²⁸ correspondingly.

We then analyzed the rate-dependent deformation behavior of nanowires by calculating the yield strain and the failure strain. As shown in Fig. 4(e), the yielding occurs earlier when the applied strain rate is reduced for both brittle and ductile nanowires. Note that the yield strain of the ductile glass significantly reduces (from $\sim 7\%$ to $\sim 3\%$), while only slightly decreasing in the brittle glass ($\sim 8\%$ to $\sim 7\%$) with the decreasing strain rate. Figure 4(f) shows that the failure strain of both brittle and ductile nanowires generally reduces as the strain rate decreases from 10^{10} to 10^0 s^{-1} . From the failure strain, we computed the rate-dependent plasticity by subtracting the elastic strain, as shown in Fig. 4(g), which is the UTS divided by Young's modulus. Interestingly, the plasticity in the brittle glass is only $\sim 2\%$ and remains unchanged with the strain rate spanning over ten orders of magnitude. In contrast, the plastic deformation inside the ductile nanowires gradually reduces from $\sim 10\%$ to $\sim 6\%$ as the strain rate decreases from $\sim 10^{11}$ to 10^0 s^{-1} . Therefore, there is an intrinsic difference between brittle and ductile nanowires with respect to the rate-dependent yielding and plasticity, which deserves further elucidation. Note that, within the timescale accessible to CMD simulations, the general agreement in mechanical properties from SLME and CMD lends support to the reliability of accelerated atomistic simulations.

DISCUSSION

Here, we aim to illustrate the atomic-level events underlying the intrinsic difference in rate-dependent yielding and plasticity in the brittle and ductile glassy nanowires as observed above. We first carried out cluster analysis to identify the severely rearranged atoms in the process of plastic deformation. Although the cluster statistics may depend on the sample size, data presented here are still valuable, given the fact that we are using exactly the same size for all nanowires.

Figure 5 shows the distribution of severely deformed clusters at a given engineering strain (6%) in the brittle and ductile nanowires from high to low strain rates. The population of severely deformed clusters increases as the loading rate reduces, which is more pronounced for the ductile nanowires. We further investigated the evolution of clusters during the plastic deformation by calculating the largest cluster size and the number of clusters. As depicted in Fig. 6(a), the largest cluster size in the brittle nanowires changes slightly with the applied strain and mostly contains ~ 50 atoms in size. Upon fracture, the largest cluster size jumps

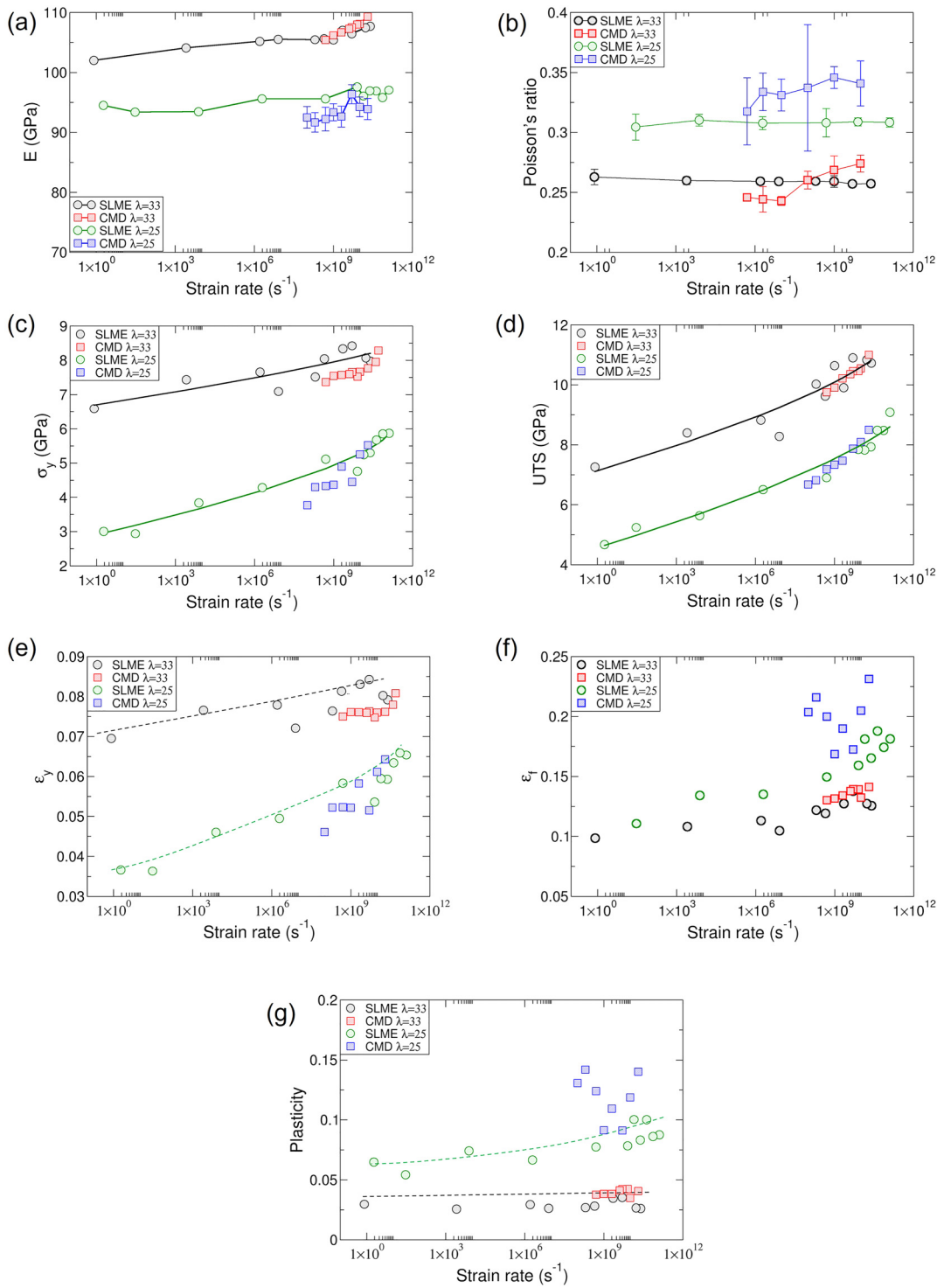


FIG. 4. (a) Young's modulus (E), (b) Poisson's ratio, (c) yield strength (σ_y), (d) the ultimate tensile strength (UTS), (e) yield strain (ϵ_y), (f) failure strain (ϵ_f), and (g) plasticity of brittle ($\lambda = 33$) and ductile ($\lambda = 25$) glassy nanowires as a function of the strain rate from SLME and CMD. The solid lines are fitted to the cooperative shear model.⁷⁰ The dashed lines merely serve as a guide to the eye.

TABLE I. Parameters in the cooperative shear model from fitting to SLME results.

	σ_0/GPa	$\frac{k_B T}{W_{T_g}} \frac{G_T}{G_{T_g}}$	W_{T_g}/J	w'_0/Hz
Brittle sample ($\lambda = 33$)	9.193	0.004	9.423×10^{-19}	7.568×10^{13}
Ductile sample ($\lambda = 25$)	5.951	0.014	2.927×10^{-19}	1.504×10^{13}

abruptly due to the creation of free surfaces, which echoes the brittleness of the tested nanowires. In contrast, under the same loading rate, the largest cluster size in the ductile nanowires increases gradually in response to incremental strain, as illustrated in Fig. 6(b). Regardless of the strain rate, the largest cluster contains ~ 1000 atoms, indicating the occurrence of percolation in the ductile nanowires. Note that fracture will not occur promptly after the percolation of severely deformed clusters, leading to the intrinsic ductile behavior of the sample.

Next, we computed the number of clusters as the deformation evolves under tension at different loading rates. The population of severely deformed clusters inside the brittle nanowire was found to remain nearly unchanged, as shown in Fig. 6(c). In contrast, the highly deformed clusters inside the ductile nanowire display

significant and consecutive multiplication behavior toward necking, as the number of clusters gradually increases with the strain, as shown in Fig. 6(d). Once necking occurs, the number of clusters, therefore, decreases sharply. Taken together, as compared with the brittle nanowire, the ductile sample displays a more pronounced strain localization with a reducing strain rate, thus leading to a more apparent reduction in yield strain and plasticity. The intrinsic difference in atomic-level plastic events, especially the rate-dependent localization behavior, in turn, leads to the difference in the mechanical response of the brittle and ductile nanowires at varying strain rates.

Finally, to build the connection between atomic-level deformation behaviors with the sampling of the PEL, we computed the nonaffine displacement matrix (NaDM), which is defined below following the previous publication.⁴⁹

$$\Delta^2(\varepsilon', \varepsilon'') = \frac{1}{N} \sum_i^N |\mathbf{R}_i(\varepsilon'') - \mathbf{F}(\varepsilon', \varepsilon'')\mathbf{R}_i(\varepsilon')|^2, \quad (5)$$

where $\mathbf{R}_i(\varepsilon')$ is the position of atom i at tensile strain ε' and the deformation gradient tensor $\mathbf{F}(\varepsilon', \varepsilon'')$ is related to the linear affine transformation from ε' to ε'' . Here, the NaDM essentially measures the average squared nonaffine displacement for the entire sample at a strain interval from ε' to ε'' so that any barrier crossing events as well as the corresponding transition pathways in the process of

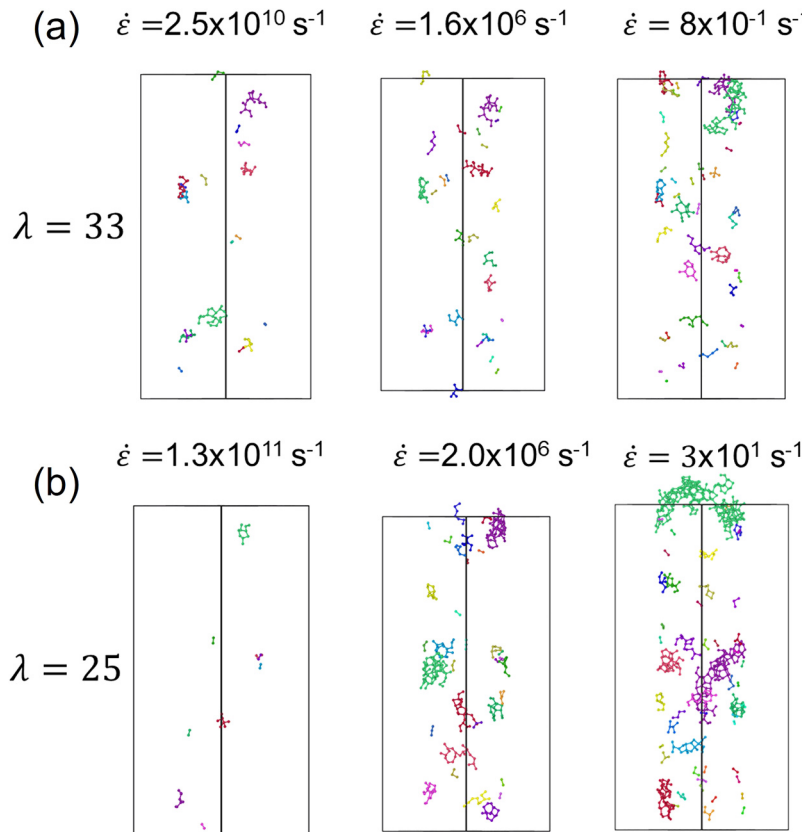


FIG. 5. Distribution of severely deformed clusters under 6% strain at different strain rates for (a) brittle ($\lambda = 33$) and (b) ductile ($\lambda = 25$) glassy nanowires. The clusters are identified with the atomic shear strain. For each sample, the clusters are color coded based on the cluster size from ~ 150 (the largest cluster) to 2 (the smallest cluster).

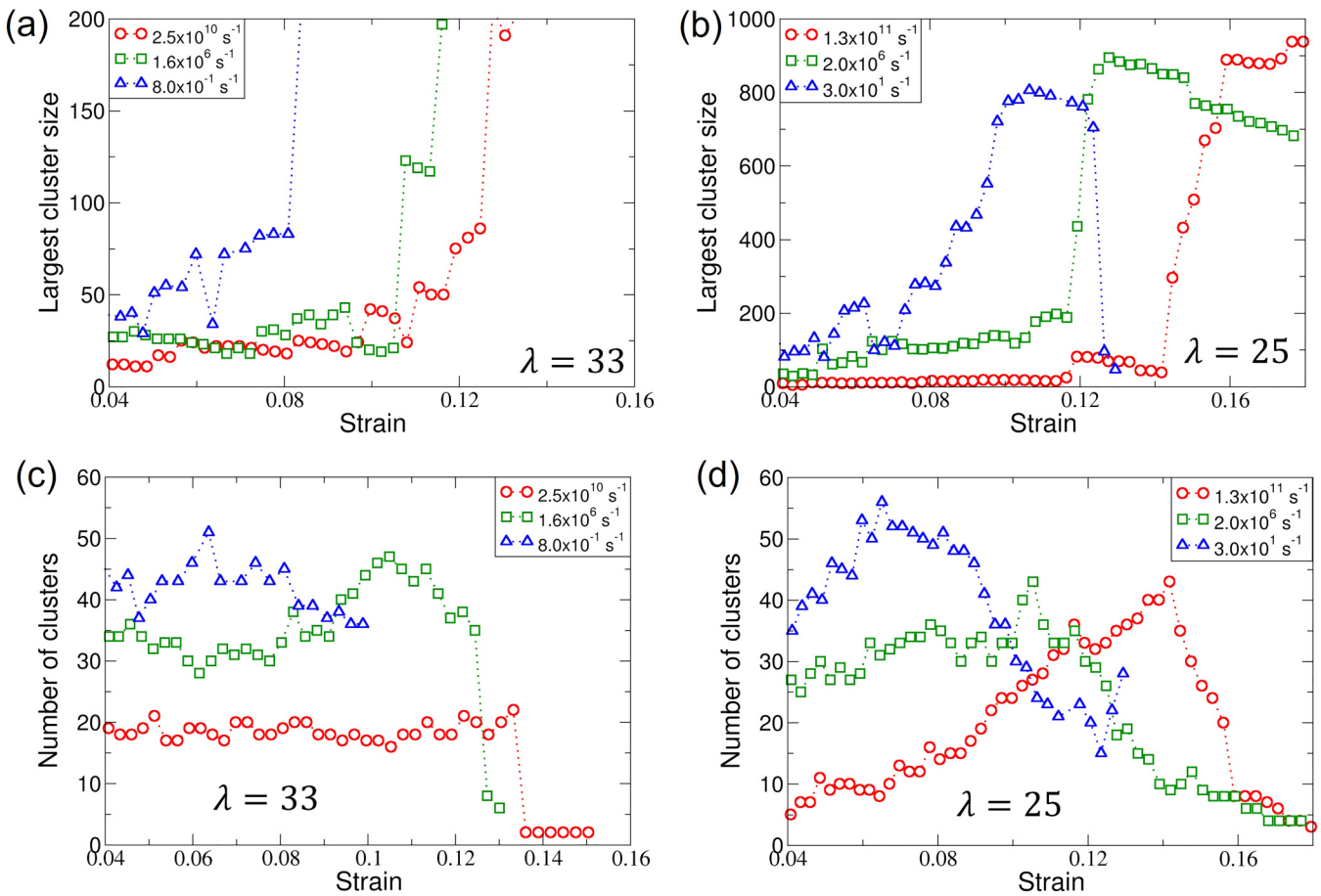


FIG. 6. The largest cluster size as a function of tensile strain under different loading rates for (a) brittle ($\lambda = 33$) and (b) ductile ($\lambda = 25$) glassy nanowires. The number of clusters as a function of tensile strain under different loading rates for (c) brittle ($\lambda = 33$) and (d) ductile ($\lambda = 25$) glassy nanowires.

mechanical deformation can be identified. In addition, by using the position matrix \mathbf{R} of the inherent structures⁷³ as we did here, any explored local basins and saddle points can be recorded and the sampled PEL can be depicted. For instance, if the system is located in the same basin on the PEL during pure elastic deformation, the calculated NaDM would be close to zero. In contrast, when the system experiences frequent barrier crossings among different local basins on the PEL in the process of plastic deformation, the computed NaDM would be more noticeable. These barrier crossing events are mainly driven by the applied stress since the tensile tests are conducted at room temperature that provides negligible thermal activation to the system.

To understand how the sampling of the PEL changes with the applied loading rate, we calculated the NaDM for both brittle and ductile glassy nanowires at selective strain rates, as shown in Fig. 7. One can see that the clustering of darkly shaded (blue) squares dominates in the graph at the high loading rate ($\dot{\epsilon} \sim 10^{10}-10^{11}\text{s}^{-1}$), which suggests that the barrier crossing events are not widely activated in both brittle and ductile glasses.

Specifically, both glasses reside in the same local basin on the PEL under the current strain interval; hence, the deformation is mostly elastic, which is consistent with the results shown in Fig. 2. At an intermediate loading rate ($\dot{\epsilon} \sim 10^6\text{s}^{-1}$), the NaDM for both brittle and ductile glasses exhibits a hierarchical structure with small dark (blue) squares embedded in lightly shaded large squares. Note that the dark squares are bridged with lightly shaded or red squares, which is related to transitions among different inherent structures. Therefore, the PEL of both brittle and ductile glasses investigated here displays a fractal-like nature, similar to the observations in a previous report on metallic glasses.⁴⁹ With a decreasing strain rate, the local basin transitions on the PEL as indicated by block-to-block crossings are more frequently observed, especially for the ductile glassy system. At the lowest strain rate ($\dot{\epsilon} \sim 10^0\text{s}^{-1}$), the NaDM for the ductile and brittle glasses looks significantly different, where the size of the dark clusters is much smaller in the ductile sample. This suggests that the ductile glass experiences more frequent barrier crossing events on the fractal PEL during tensile deformation, resulting in a more severe rearrangement of

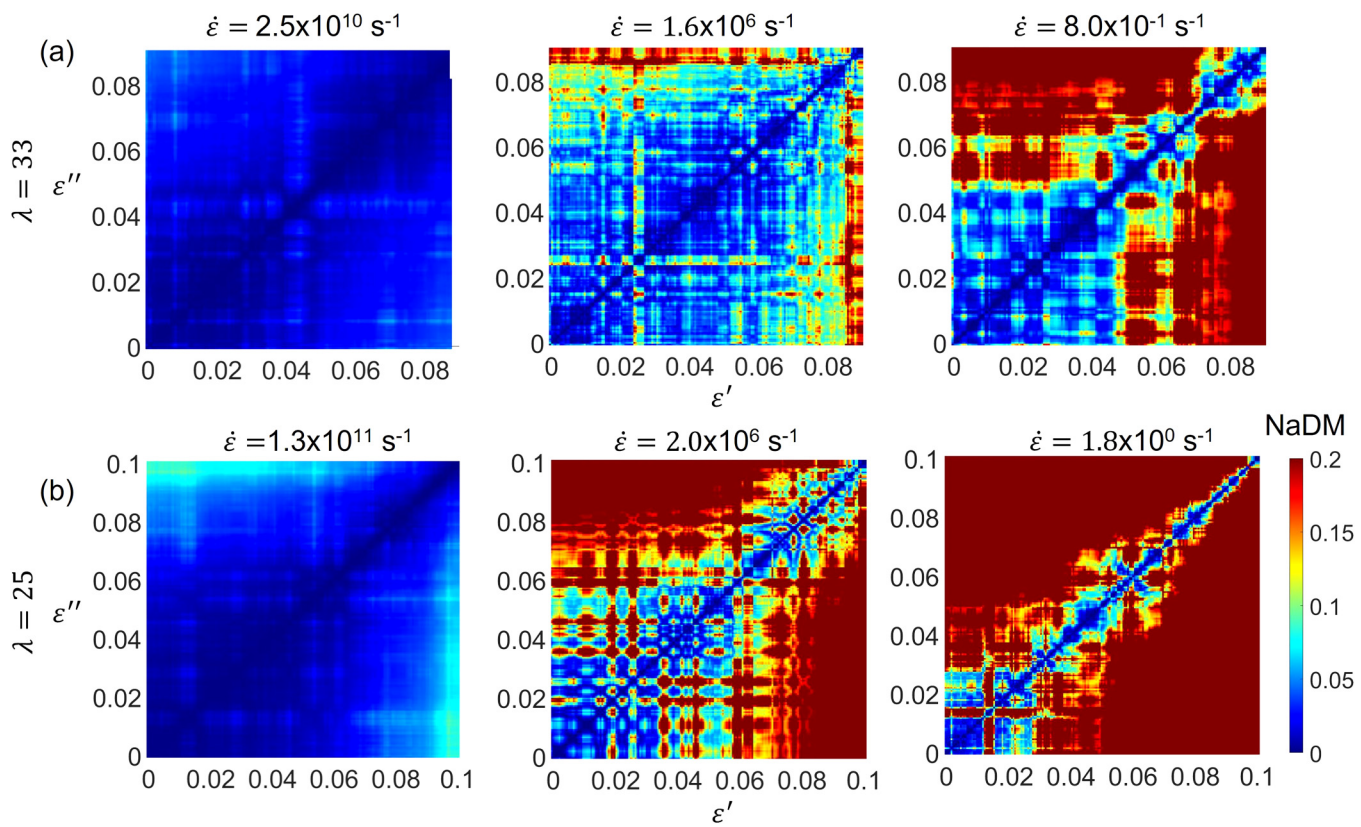


FIG. 7. NaDM $\Delta^2(\varepsilon', \varepsilon'')$ for inherent structures visited sequentially under tension in (a) brittle ($\lambda = 33$) and (b) ductile ($\lambda = 25$) glassy nanowires at different strain rates. The color coding is based on the NaDM values calculated in Eq. (5).

atoms and, thus, earlier yielding behavior. Therefore, the smaller yield strain in ductile glass over the applied strain-rate regime is due to the higher likelihood for the system to escape from a metabasin. In addition, the more frequent basin transitions on the PEL with reducing the strain rate are also responsible for the more apparent reduction in the yield strain and plasticity in the ductile glass, as shown in Figs. 4(e) and 4(g).

The contrast in the NaDM for the ductile and brittle systems signifies an intrinsic difference in the hierarchical structure of their PEL. To further characterize the hierarchy of the visited landscape, we computed the average squared nonaffine displacement (ASNaD) following the previous publication⁴⁹ as defined below:

$$\delta^2(\varepsilon, \xi) = \Delta^2(\varepsilon, \varepsilon + \xi). \quad (6)$$

This corresponds to the quantity along the diagonal of the NaDM over a strain lapse ξ at strain ε . Note that the ASNaD computed here can, in fact, be used to depict the structure of one-dimensional PEL along the sampling direction.

As shown in Figs. 8(a) and 8(b), the ASNaD changes from small peaks to medium peaks embedded with large peaks when the strain rate decreases for both brittle and ductile glasses. Here, the

peak heights are closely related to the activation energy barriers for the local transitions. The small peaks (height < 0.01) stem from the localized barrier crossing events, where only a few atomic-level plastic events are involved, as shown in Fig. 8(c). The medium and high peaks (height > 0.1) originate from a series of barrier crossings and even metabasin escaping events on the PEL, where more pronounced atomic rearrangements are involved, as seen in Fig. 8(d). Those barrier crossing and metabasin escaping events are prevalent in the ductile glass, thus indicating a more complex hierarchical structure of the PEL. Based on the ASNaD at the lowest strain rate, we depicted and compared the PEL of the brittle and ductile glasses along the sampling direction, as in Fig. 9. Particularly, we reveal that the metabasins in the ductile glass are rougher (consisting of many small minima), narrower, and shallower, making it easier to trigger atomic rearrangements and plastic deformation. As for the brittle glass, the metabasins on the PEL are smoother, wider, and deeper, giving rise to higher activation energy barriers that inhibit plastic deformation. In other words, for a glass with a more hierarchical PEL, the system has a higher probability to explore more minima on the PEL with a reducing strain rate, which increases the propensity of strain localization. Therefore, the intrinsically different rate-dependent yielding and plasticity of the brittle and ductile glasses

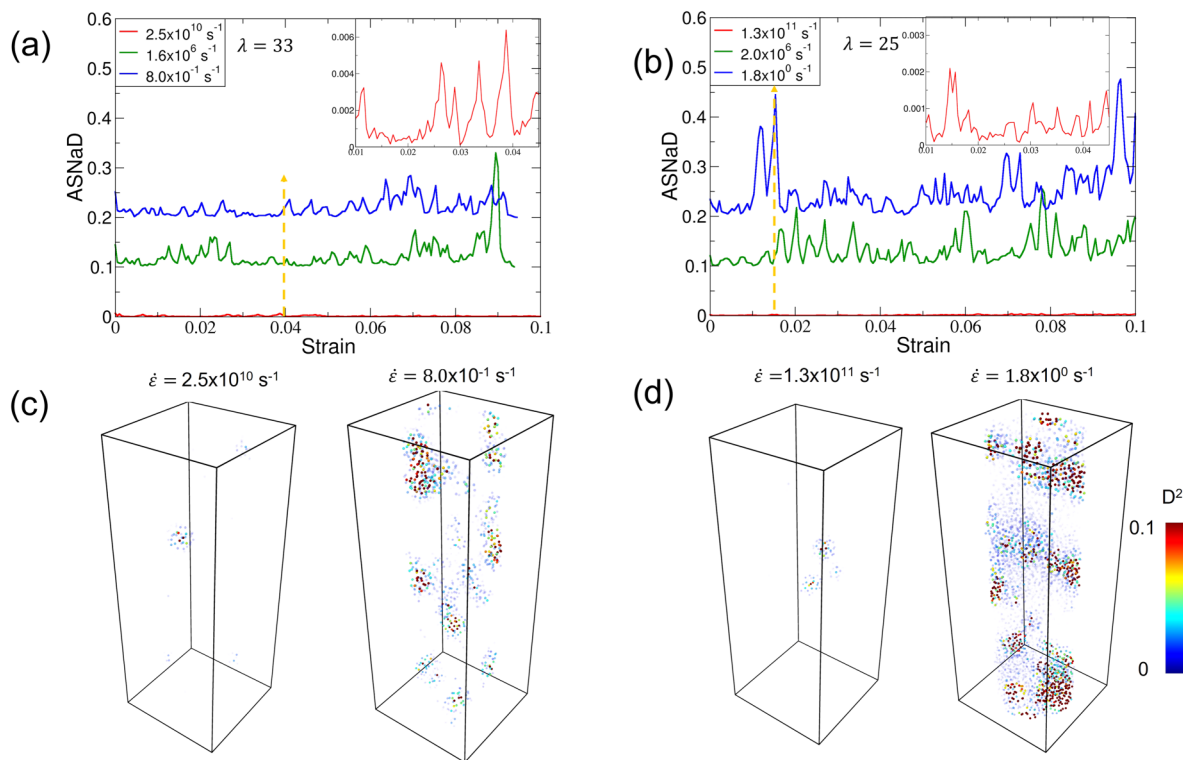


FIG. 8. ASNaD of (a) brittle ($\lambda = 33$) and (b) ductile ($\lambda = 25$) glassy nanowires at three representative strain rates. The green and blue curves are shifted upward by 0.1 and 0.2, respectively, for clarity. A zoom-in of the red curve in the low strain range is shown as insets in (a) and (b). Spatial distributions of severely deformed clusters for barrier crossing events under a given strain [indicated by a yellow arrow in (a) and (b)] at two extreme strain rates for (c) brittle and (d) ductile glasses. The color coding is based on the nonaffine deformation (D^2). Atoms with low D^2 are set to be transparent for clarity.

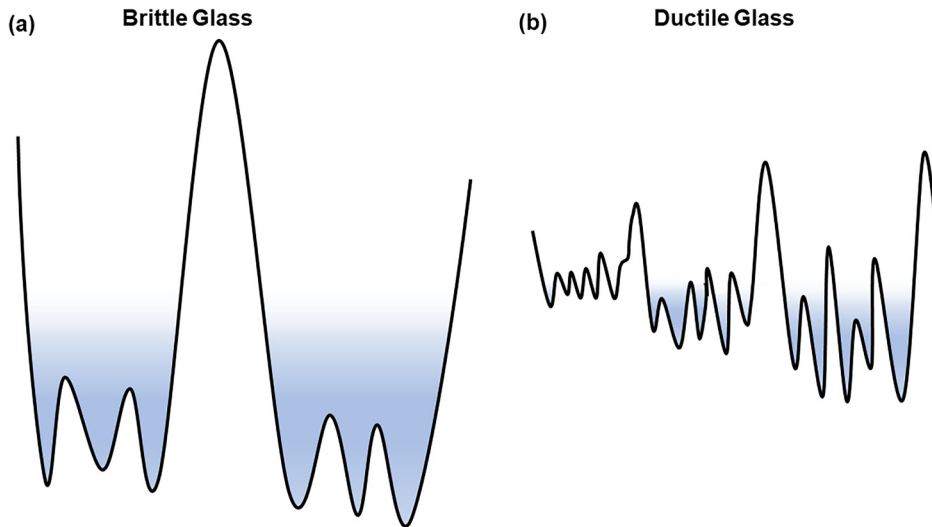


FIG. 9. Schematics of a 1D fractal PEL with strain rate determined barrier crossing events for (a) brittle ($\lambda = 33$) and (b) ductile ($\lambda = 25$) glasses.

originate from the distinct hierarchy of their fractal PEL. The fractal PEL depicted here can be very useful for understanding the intrinsic brittleness/ductility of glassy materials.

CONCLUSIONS

Using accelerated atomistic simulations based on the SLME algorithm to access timescales close to experiments, we systematically studied the strain-rate-dependent mechanical properties and uncovered the underlying deformation mechanisms of brittle and ductile silicon glassy nanowires under strain rates spanning over ten orders of magnitude. While the yield strain and the plasticity of brittle nanowires remain almost unchanged, they noticeably decrease with reducing the strain rate in ductile nanowires due to the high-strain localization propensity resulting from the more hierarchical potential energy landscape. Our study provides valuable insights into understanding the intrinsic ductility of glassy materials, which is of critical importance for applications in emerging devices such as nanoresonators and nanoswitches.

ACKNOWLEDGMENTS

This work was supported by the National Science Foundation (NSF) under Grant Nos. DMR-1508410, DMR-1936368, and DMR-2015557. P.C. acknowledges support from the Department of Mechanical and Aerospace Engineering, University of California, Irvine. MD simulations were carried out on supercomputers at the Center for Computational Innovations (CCI) at the RPI.

DATA AVAILABILITY

The data that support the findings of this study are available from the corresponding author upon reasonable request.

REFERENCES

- ¹D. P. Yu *et al.*, “Amorphous silica nanowires: Intensive blue light emitters,” *Appl. Phys. Lett.* **73**, 3076–3078 (1998).
- ²L.-F. Cui, R. Ruffo, C. K. Chan, H. Peng, and Y. Cui, “Crystalline-amorphous core-shell silicon nanowires for high capacity and high current battery electrodes,” *Nano Lett.* **9**, 491–495 (2009).
- ³J. Zhu *et al.*, “Optical absorption enhancement in amorphous silicon nanowire and nanocone arrays,” *Nano Lett.* **9**, 279–282 (2009).
- ⁴Y. Chen *et al.*, “Phase engineering of nanomaterials,” *Nat. Rev. Chem.* **4**, 243–256 (2020).
- ⁵R. Ramachandramoorthy, W. Gao, R. Bernal, and H. Espinosa, “High strain rate tensile testing of silver nanowires: Rate-dependent brittle-to-ductile transition,” *Nano Lett.* **16**, 255–263 (2016).
- ⁶Y. Zhang, L. Huang, and Y. Shi, “Silica glass toughened by consolidation of glassy nanoparticles,” *Nano Lett.* **19**, 5222–5228 (2019).
- ⁷R. Ramachandramoorthy *et al.*, “Dynamic plasticity and failure of microscale glass: Rate-dependent ductile–brittle–ductile transition,” *Nano Lett.* **19**, 2350–2359 (2019).
- ⁸L. Wondraczek *et al.*, “Towards ultrastrong glasses,” *Adv. Mater.* **23**, 4578–4586 (2011).
- ⁹M. Ashby and A. Greer, “Metallic glasses as structural materials,” *Scr. Mater.* **54**, 321–326 (2006).
- ¹⁰B. Deng, J. Luo, J. T. Harris, C. M. Smith, and M. E. McKenzie, “Molecular dynamics simulations on fracture toughness of $\text{Al}_2\text{O}_3\text{-SiO}_2$ glass-ceramics,” *Scr. Mater.* **162**, 277–280 (2019).
- ¹¹H. Guo *et al.*, “Tensile ductility and necking of metallic glass,” *Nat. Mater.* **6**, 735–739 (2007).
- ¹²J. Luo *et al.*, “Size-dependent brittle-to-ductile transition in silica glass nanofibers,” *Nano Lett.* **16**, 105–113 (2016).
- ¹³J. J. Lewandowski, W. H. Wang, and A. L. Greer, “Intrinsic plasticity or brittleness of metallic glasses,” *Philos. Mag. Lett.* **85**, 77–87 (2005).
- ¹⁴Y. Shi, J. Luo, F. Yuan, and L. Huang, “Intrinsic ductility of glassy solids,” *J. Appl. Phys.* **115**, 043528 (2014).
- ¹⁵D. Jang and J. R. Greer, “Transition from a strong-yet-brittle to a stronger-and-ductile state by size reduction of metallic glasses,” *Nat. Mater.* **9**, 215–219 (2010).
- ¹⁶Y. Shi, “Size-dependent mechanical responses of metallic glasses,” *Int. Mater. Rev.* **64**, 163–180 (2019).
- ¹⁷D. Sopu, A. Foroughi, M. Stoica, and J. Eckert, “Brittle-to-ductile transition in metallic glass nanowires,” *Nano Lett.* **16**, 4467–4471 (2016).
- ¹⁸Y. Shi, “Size-independent shear band formation in amorphous nanowires made from simulated casting,” *Appl. Phys. Lett.* **96**, 121909 (2010).
- ¹⁹J. R. Trelewicz and C. A. Schuh, “The Hall-Petch breakdown at high strain rates: Optimizing nanocrystalline grain size for impact applications,” *Appl. Phys. Lett.* **93**, 171916 (2008).
- ²⁰Z. C. Cordero, B. E. Knight, and C. A. Schuh, “Six decades of the Hall-Petch effect—A survey of grain-size strengthening studies on pure metals,” *Int. Mater. Rev.* **61**, 495–512 (2016).
- ²¹J. S. Langer, “Shear-transformation-zone theory of plastic deformation near the glass transition,” *Phys. Rev. E* **77**, 021502 (2008).
- ²²A. S. Argon, “Plastic deformation in metallic glasses,” *Acta Metall.* **27**, 47–58 (1979).
- ²³C. Fusco, T. Albaret, and A. Tanguy, “Role of local order in the small-scale plasticity of model amorphous materials,” *Phys. Rev. E* **82**, 066116 (2010).
- ²⁴Y. Shi, M. B. Katz, H. Li, and M. L. Falk, “Evaluation of the disorder temperature and free-volume formalisms via simulations of shear banding in amorphous solids,” *Phys. Rev. Lett.* **98**, 185505 (2007).
- ²⁵M. Sansa, “Frequency fluctuations in silicon nanoresonators,” *Nat. Nanotechnol.* **11**, 552 (2016).
- ²⁶T. Xu, Y.-K. Wu, X. Luo, and L. J. Guo, “Plasmonic nanoresonators for high-resolution colour filtering and spectral imaging,” *Nat. Commun.* **1**, 59 (2010).
- ²⁷V. V. Deshpande *et al.*, “Carbon nanotube linear bearing nanoswitches,” *Nano Lett.* **6**, 1092–1095 (2006).
- ²⁸F. Yuan and L. Huang, “Molecular dynamics simulation of amorphous silica under uniaxial tension: From bulk to nanowire,” *J. Non-Cryst. Solids* **358**, 3481–3487 (2012).
- ²⁹Y. Q. Cheng and E. Ma, “Intrinsic shear strength of metallic glass,” *Acta Mater.* **59**, 1800–1807 (2011).
- ³⁰K. Albe, Y. Ritter, and D. Sopu, “Enhancing the plasticity of metallic glasses: Shear band formation, nanocomposites and nanoglasses investigated by molecular dynamics simulations,” *Mech. Mater.* **67**, 94–103 (2013).
- ³¹Y. Zhang *et al.*, “Design ductile and work-hardenable composites with all brittle constituents,” *Acta Mater.* **208**, 116770 (2021).
- ³²Y. Zhang, L. Huang, and Y. Shi, “Towards damage resistant $\text{Al}_2\text{O}_3\text{-SiO}_2$ glasses with structural and chemical heterogeneities through consolidation of glassy nanoparticles,” *Acta Mater.* **215**, 117016 (2021).
- ³³L. Tian, Z.-W. Shan, and E. Ma, “Ductile necking behavior of nanoscale metallic glasses under uniaxial tension at room temperature,” *Acta Mater.* **61**, 4823–4830 (2013).
- ³⁴Y. Yue and K. Zheng, “Strong strain rate effect on the plasticity of amorphous silica nanowires,” *Appl. Phys. Lett.* **104**, 231906 (2014).
- ³⁵M. L. Manning, E. G. Daub, J. S. Langer, and J. M. Carlson, “Rate-dependent shear bands in a shear-transformation-zone model of amorphous solids,” *Phys. Rev. E* **79**, 016110 (2009).
- ³⁶J. Lu, G. Ravichandran, and W. L. Johnson, “Deformation behavior of the $\text{Zr}_{41.2}\text{Ti}_{13.8}\text{Cu}_{12.5}\text{Ni}_{10}\text{Be}_{22.5}$ bulk metallic glass over a wide range of strain-rates and temperatures,” *Acta Mater.* **51**, 3429–3443 (2003).

³⁷C. A. Schuh, A. C. Lund, and T. G. Nieh, "New regime of homogeneous flow in the deformation map of metallic glasses: Elevated temperature nanoindentation experiments and mechanistic modeling," *Acta Mater.* **52**, 5879–5891 (2004).

³⁸G. T. Barkema and N. Mousseau, "Event-based relaxation of continuous disordered systems," *Phys. Rev. Lett.* **77**, 4358–4361 (1996).

³⁹G. Henkelman and H. Jónsson, "A dimer method for finding saddle points on high dimensional potential surfaces using only first derivatives," *J. Chem. Phys.* **111**, 7010–7022 (1999).

⁴⁰A. F. Voter, "Hyperdynamics: Accelerated molecular dynamics of infrequent events," *Phys. Rev. Lett.* **78**, 3908–3911 (1997).

⁴¹M. R. So/rensen and A. F. Voter, "Temperature-accelerated dynamics for simulation of infrequent events," *J. Chem. Phys.* **112**, 9599–9606 (2000).

⁴²A. Kushima *et al.*, "Computing the viscosity of supercooled liquids," *J. Chem. Phys.* **130**, 224504 (2009).

⁴³Y. Fan and P. Cao, "Long time-scale atomistic modeling and simulation of deformation and flow in solids," in *Handbook of Materials Modeling*, edited by W. Andreoni and S. Yip (Springer International Publishing, 2019), pp. 1–27.

⁴⁴P. Cao, M. Li, R. J. Heugle, H. S. Park, and X. Lin, "Self-learning metabasin escape algorithm for supercooled liquids," *Phys. Rev. E* **86**, 016710 (2012).

⁴⁵P. Cao, H. S. Park, and X. Lin, "Strain-rate and temperature-driven transition in the shear transformation zone for two-dimensional amorphous solids," *Phys. Rev. E* **88**, 042404 (2013).

⁴⁶X. Yan, P. Cao, W. Tao, P. Sharma, and H. S. Park, "Atomistic modeling at experimental strain rates and timescales," *J. Phys. Appl. Phys.* **49**, 493002 (2016).

⁴⁷W. Tao, P. Cao, and H. S. Park, "Atomistic simulation of the rate-dependent ductile-to-brittle failure transition in bicrystalline metal nanowires," *Nano Lett.* **18**, 1296–1304 (2018).

⁴⁸P. Cao, M. P. Short, and S. Yip, "Understanding the mechanisms of amorphous creep through molecular simulation," *Proc. Natl. Acad. Sci. U.S.A.* **114**, 13631–13636 (2017).

⁴⁹P. Cao, M. P. Short, and S. Yip, "Potential energy landscape activations governing plastic flows in glass rheology," *Proc. Natl. Acad. Sci. U.S.A.* **116**, 18790–18797 (2019).

⁵⁰S. Plimpton, "Fast parallel algorithms for short-range molecular dynamics," *J. Comput. Phys.* **117**, 1–19 (1995).

⁵¹S. Nosé, "A molecular dynamics method for simulations in the canonical ensemble," *Mol. Phys.* **52**, 255–268 (1984).

⁵²W. G. Hoover, "Canonical dynamics: Equilibrium phase-space distributions," *Phys. Rev. A* **31**, 1695–1697 (1985).

⁵³F. H. Stillinger and T. A. Weber, "Computer simulation of local order in condensed phases of silicon," *Phys. Rev. B* **31**, 5262–5271 (1985).

⁵⁴M. J. Demkowicz and A. S. Argon, "High-density liquidlike component facilitates plastic flow in a model amorphous silicon system," *Phys. Rev. Lett.* **93**, 025505 (2004).

⁵⁵V. Molinero, S. Sastry, and C. A. Angell, "Tuning of tetrahedrality in a silicon potential yields a series of monatomic (metal-like) glass formers of very high fragility," *Phys. Rev. Lett.* **97**, 075701 (2006).

⁵⁶A. Stukowski, "Visualization and analysis of atomistic simulation data with OVITO—The open visualization tool," *Model. Simul. Mater. Sci. Eng.* **18**, 015012 (2010).

⁵⁷M. L. Falk and J. S. Langer, "Dynamics of viscoplastic deformation in amorphous solids," *Phys. Rev. E* **57**, 7192–7205 (1998).

⁵⁸Y. Fan, Y. N. Osetskiy, S. Yip, and B. Yildiz, "Mapping strain rate dependence of dislocation-defect interactions by atomistic simulations," *Proc. Natl. Acad. Sci. U.S.A.* **110**, 17756–17761 (2013).

⁵⁹A. F. Voter, F. Montalenti, and T. C. Germann, "Extending the time scale in atomistic simulation of materials," *Annu. Rev. Mater. Res.* **32**, 321–346 (2002).

⁶⁰D. Perez, E. D. Cubuk, A. Waterland, E. Kaxiras, and A. F. Voter, "Long-time dynamics through parallel trajectory splicing," *J. Chem. Theory Comput.* **12**, 18–28 (2016).

⁶¹R. Fletcher and M. J. D. Powell, "A rapidly convergent descent method for minimization," *Comput. J.* **6**, 163–168 (1963).

⁶²N. Metropolis, A. W. Rosenbluth, M. N. Rosenbluth, A. H. Teller, and E. Teller, "Equation of state calculations by fast computing machines," *J. Chem. Phys.* **21**, 1087 (1953).

⁶³T. Zhu, J. Li, A. Samanta, A. Leach, and K. Gall, "Temperature and strain-rate dependence of surface dislocation nucleation," *Phys. Rev. Lett.* **100**, 025502 (2008).

⁶⁴P. Cao, X. Lin, and H. S. Park, "Strain-rate and temperature dependence of yield stress of amorphous solids via a self-learning metabasin escape algorithm," *J. Mech. Phys. Solids* **68**, 239–250 (2014).

⁶⁵W. H. Jiang *et al.*, "Rate dependence of shear banding and serrated flows in a bulk metallic glass," *J. Mater. Res.* **21**, 2164–2167 (2006).

⁶⁶C. A. Schuh and T. G. Nieh, "A nanoindentation study of serrated flow in bulk metallic glasses," *Acta Mater.* **51**, 87–99 (2003).

⁶⁷T. To *et al.*, "Fracture toughness of a metal-organic framework glass," *Nat. Commun.* **11**, 2593 (2020).

⁶⁸Y. Shi and M. L. Falk, "Atomic-scale simulations of strain localization in three-dimensional model amorphous solids," *Phys. Rev. B* **73**, 214201 (2006).

⁶⁹D. Pan, A. Inoue, T. Sakurai, and M. W. Chen, "Experimental characterization of shear transformation zones for plastic flow of bulk metallic glasses," *Proc. Natl. Acad. Sci. U.S.A.* **105**, 14769–14772 (2008).

⁷⁰M. D. Demetriou *et al.*, "Cooperative shear model for the rheology of glass-forming metallic liquids," *Phys. Rev. Lett.* **97**, 065502 (2006).

⁷¹W. L. Johnson and K. Samwer, "A universal criterion for plastic yielding of metallic glasses with a $(T/T_g)^{2/3}$ temperature dependence," *Phys. Rev. Lett.* **95**, 195501 (2005).

⁷²R. H. Doremus, "Viscosity of silica," *J. Appl. Phys.* **92**, 7619–7629 (2002).

⁷³P. G. Debenedetti and F. H. Stillinger, "Supercooled liquids and the glass transition," *Nature* **410**, 259–267 (2001).